International Forum on Aeroelasticity and Structural Dynamics
IFASD 2024
17-21 June 2024, The Hague, The Netherlands

EFFECT OF FLOW SEPARATION ON DISCRETE GUST LOADS FOR A FREE-FLYING ELASTIC AIRCRAFT

Johan M. Feldwisch[1]

[1]German Aerospace Center (DLR) - Institute of Aeroelasticity
Bunsenstr. 10, 37073 Göttingen, Germany
johan.feldwisch@dlr.de

Keywords: gust loads, flow separation, loads, transonic aerodynamics, numerical aeroelasticity, CFD, CRM,

Abstract: Shock motion and flow separation are aerodynamic nonlinearities, which have a significant effect on dynamic gust loads but are not accounted for in time-linearized aerodynamic models. Gust disturbances are not necessarily small and may cause local regions with flow separation during the gust encounter. The detached flow limits the total lift which is promising for a passive reduction of aerodynamic loads. This potentially yields lighter load carrying structures which in turn may improve the overall aircraft performance. This work investigates the reduction of distributed gust loads due to detached flow for an elastic, free-flying aircraft in an open-loop simulation with discrete gust disturbances defined by CS25. The DLR TAU-Code is utilized to solve the URANS equations. Different turbulence models (Spalart-Allmaras, RSM SSG/LRR-lnω) are applied, as predicting the flow separation correctly remains a problem. The time-linearized solution serves as reference and is obtained by scaling the time-marching responses to small gust amplitudes at the same gust gradients. The nonlinear simulation results are compared with the linear solution, to assess the potential of the load reduction. The investigated transport aircraft is the NASA Common Research model. The results show that the SA and RSM predict similar loads for cases with attached flow. For medium to long gust gradients large regions of the outer wing show flow separation during the gust encounter. Even though simulations with both turbulence models predict large regions with detached flow, the dynamics of the shock motion and the flow separation are different. The SA turbulence model predicts drastic changes of the aerodynamic loads at the wing tip and thus excites structural oscillations which are not seen with the RSM. A reduction of the maximum root bending moment between -16% to -24% is found for the RSM compared to the time-linearized solution. For the SA turbulence model, this deviation is in the range of -21% to -29%.

1 MOTIVATION

Structural components and hence the operating empty mass of an aircraft are significantly driven by maneuver and gust loads. While most maneuver loads cases can be treated as quasi-steady bookcases, in which a quasi-steady nonlinear aerodynamic surrogate model can be used, gust loads are based on time-linearized aerodynamics. Thus, the aerodynamic system is treated as time-invariant, which is a questionable assumption for cases with strong shock motion and even flow separation.

In [1] differences between the time-linearized and nonlinear time-marching have been investigated on the CRM configuration for discrete gusts in CS-25 relevant parameter space. The

simulations were conducted with the DLR TAU-Code and the aeroelastic degrees of freedom were heave, pitch and first wing bending modes. With increasing gust amplitude, the maximum root bending moment of the nonlinear simulation reduces compared to the linear solution. The main cause for the differences was explained linear method, which cannot account for shock motion.

Further investigation of the nonlinear aerodynamic effects at larger gust amplitudes are provided in [2]. Here, harmonically oscillating gust fields were analyzed in a pure aerodynamic simulation using the DLR TAU Code without any motion or deformation. The main focus was put on the maximum global lift coefficients over the reduced frequency of the gust. It could be shown that the flow separation contributed mainly to the reduction of the maximum lift compared to the time-linearized solution. Furthermore, it was observed that the initial shock system changed significantly during the gust encounter leading to larger loads in some cases, in which flow separation were not dominant. The Spalart-Allmaras original turbulence and the RSM SSG/LRR-$\ln\omega$ turbulence model were used for the simulations. It was shown, that the RSM predicted higher maximum lift coefficients for large gust gradients. Furthermore, the time signals of the RSM look smoother compared to the SA model. Interestingly, the flow separation for the RSM was observed to remain in the rear part of the wing, while the SA turbulence model predicts flow separation over a large portion of the outboard surface of the wing up to the leading edge.

As outlined, past studies have shown that the assumption of time-linearized aerodynamics is questionable at transonic speeds where strong shock motion and flow separation occur. This paper focuses on the nonlinear effect due to flow separation on loads for a free flying, elastic aircraft. As the time signals of the different turbulence models and the affected region with detached flow in [2] show qualitative differences, it is of interest to determine the influence of those effects on the structural response and the total loads.

2 MODELS

The NASA Common Research model (CRM) provides a geometry for a transport aircraft with a fuselage, horizontal tail plane, a wing and an engine nacelle. It was developed by Vassberg et al. [3] to serve as an aerodynamic reference case for simulations and wind-tunnels. The CRM was used in multiple aerodynamic drag prediction workshops and further geometries are derived from it. A projected wing area of $S_{ref} = 385\,\mathrm{m}^2$, a span of $b = 58.76\,\mathrm{m}$ and a mean aerodynamic chord of $MAC = 7.005\,\mathrm{m}$ are used as geometric reference quantities. The normalized span wise position is defined by $\eta := \frac{2y}{b}$. One structural model for the CRM is the FERMAT configuration provided by Klimmek [4] as an MSC.Nastran model.

This FERMAT model has been used to determine a jig-shape, which has been applied to the aerodynamic shape in [5]. For this work, the hybrid, unstructured mesh provided by [5] is jointly used with the FERMAT-C8 model. The CFD mesh contains surfaces for the fuselage, the horizontal tail plane, the wing, a pylon and a flow-through nacelle. The full mesh consists of about 14,000,000 nodes and the surface mesh of 275,000 nodes, which is coarse but has been shown to be satisfactory for the flow separation effects of interest [2].

The maximum take off mass of the FERMAT-C8 configuration is 260 tons, the center of gravity is positioned relatively to the fuselage nose at $x = 31.345\,\mathrm{m}$ and $z = 0.450\,\mathrm{m}$. The inertia tensor at the center of gravity consists of $I_{xx} = 1.698 \times 10^7\,\mathrm{kg\,m}^2$, $I_{yy} = 2.579 \times 10^7\,\mathrm{kg\,m}^2$, $I_{zz} = 4.144 \times 10^7\,\mathrm{kg\,m}^2$, $I_{xz} = -1.348 \times 10^6\,\mathrm{kg\,m}^2$. For this study, the first 44 elastic modes

are considered spanning a frequency range from $f_7 = 1.062\,\mathrm{Hz}$ to $f_{50} = 23.573\,\mathrm{Hz}$. The rigid body modes are synthetically generated for each rigid body degree of freedom.

The coupling model is generated by slicing the CFD-surface mesh at the location of the so called loads reference axis (LRA). The normal vectors for the cuts have been chosen such that the coupling points are aligned with the orientation of the ribs. There is a small range at the wings kink, where the orientation is smoothly titled towards the inner ribs, which are aligned parallel to the flow. The extracted points from the slice are down-sampled to meet a similar chord-wise as span-wise resolution. The CFD-surface mesh, the finite element model, the extracted coupling nodes and the loads reference axis are shown in Figure 1. Several sparse matrices for rigid splines and integration matrices are setup based on the different spatial models. Thus, transfer of loads between those model is achieved by a chained matrix operation. While the transfer of loads from the CFD mesh to the coupling model is based on nearest neighbors, the transfer of nodal displacements in the opposite direction is achieved by radial basis functions.

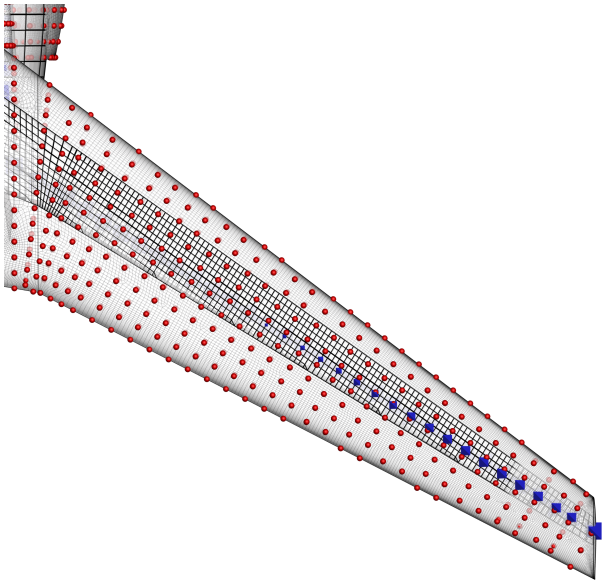

Figure 1: CFD surface mesh, FEM mesh, red coupling points which are attached to the loads reference axis in blue.

3 SIMULATION PROCESSES

3.1 The simulation environment

The CFD-based aeroelastic simulations are executed with UltraFLoads, a python based framework for aeroelastic simulations which orchestrates several Plug-ins and tools in the FlowSimulator [6]. The FlowSimulator is an open software platform, jointly developed by Airbus, Onera and DLR for high fidelity simulations involving CFD [7, 8]. The utilized CFD solver is the DLR TAU Code for solving the unsteady Reynolds-Averaged Navier–Stokes (uRANS) equations with various turbulence models. It was designed for the simulation of transport aircraft in transonic flow. The DLR TAU Code is an edge-based unstructured solver, using the dual-grid approach and works with hybrid meshes. More details about the DLR TAU Code can be found in [9, 10]. TAU accounts for grid velocities from rigid body motion, external gust disturbances (field velocity method) and grid motion due to mesh deformation by backwards differencing CFD grid point coordinates of previous time steps.

3.2 Turbulence models

For the solution of the RANS equations, the symmetric Reynolds stress tensor with 6 unknowns must be modeled. In this study, the Reynolds stress model (RSM) SSG/LRR-$\ln \omega$ model is used, which solves additional 6 transport equations for the Reynolds stresses and one equation for the length scale ω [11, 12]. The Spalart-Allmaras negative (SA-neg) [13] is a simpler model, which solves one transport equation for the turbulent eddy viscosity. For this study, the QRC extension has been used for the SA-neg turbulence model. In the following, the turbulence models are referred to by RSM and SA. A summary of the 6th Drag Prediction Workshop is given in [14], where steady results of the different turbulence models and wind tunnel experiments are compared for the CRM. From the results it can be seen, that the turbulence models and the wind tunnel experiments predict very similar steady $\partial C_L/\partial\alpha$ slopes, but the C_{L0} do not agree. Hence, the comparisons should be based on the same C_L rather than on the same α.

3.3 Equation of motion

The structural degrees of freedom $u(t)$ are approximated by a reduced set of structural modes which are based on an unconstrained Finite-Element model. The generalized equation of motion is then

$$M_{hh}\ddot{q}_h + B_{hh}\dot{q}_h + K_{hh}q_h = L_h(q_h, \dot{q}_h, \xi, t), \tag{1}$$

where M_{hh}, B_{hh}, K_{hh}, L_h and q_h are generalized matrices for mass, damping, stiffness, generalized loads and generalized coordinates. In this work, no structural damping is considered so $B_{hh} = 0$. Further parameters like actuators or disturbances are aggregated in the vector ξ. The equation of motion is solved for rigid and elastic modes, such that it solves the linearized flight dynamic equations as well. The elastic modes, the mass matrix and stiffness matrix are extracted from a modal analysis with MSC.Nastran using a maximum displacement normalization for the structural modes. The flight dynamic mass matrix is then used as modal mass for the synthetic modes. The generalized aerodynamic loads $L_h^{\text{aero}}(q_h, \dot{q}_h, \xi, t)$ are not time-linearized so they appear on the right-hand-side. The equations of motion are coupled through the aerodynamic forces, which implicitly depend on the generalized motion.

3.4 Aeroelastic equilibrium

For the steady aerostructural equilibrium the structural acceleration $\ddot{q}_h$ and velocities $\dot{q}_h$ are set to zero, so the generalized coordinates q_h for the elastic modes can be solved directly with

$$q_h = K_{hh}^{-1} L_h(q_h, \xi). \tag{2}$$

This implicit problem is solved iteratively in a loosely coupled loop.

3.5 Trim process

Time domain gust loads computations must start from a steady state reference solution. A trim solver is used to find the flight mechanic equilibrium Eq. 2 in an outer loop, while the aeroelastic equilibrium is solved in an inner loop [6]. The trim solvers reaches the steady state solution by varying the angle of attack α and the rotation of the horizontal tail plane η_{HTP}. The results are the relevant steady state flow quantities, the steady deformation, α and η_{HTP}.

3.6 Discrete gusts

Focus of this study are vertical discrete gusts (1-cos), which are parametrized by the gust gradient H and the gust amplitude w_{g} according to CS25.341(a) in [15]

$$w(t) = \frac{1}{2} w_{\text{g}} (1 - \cos(\frac{\pi t U_\infty}{H})) \quad t \in [0, 2H/U_\infty] \quad \text{and} \quad w(t) = 0m/s \quad t > 2H/U_\infty. \tag{3}$$

The gust amplitude w_g is the product of the reference velocity w_{ref} (Table 1) and the flight profile alleviation factor $F_g \leq 1$. The table also shows, the investigated gust gradients of this work. In this study, F_g is just use as a scaling factor of the gust amplitudes.

Table 1: Gust gradients and reference amplitudes (TAS) at an altitude of $10668m$.

$H\ /m$	$w_{ref}\ /ms^{-1}$
10	12.47
30	14.98
60	16.81
90	17.99
100	18.31

A visualization of the gust disturbance velocity w over the non-dimensional convection time $\tau = tU_\infty/MAC$ is shown in Figure 2. The figure shows the gust disturbance velocity at the intersection between the wings leading edge and the fuselage. The gust disturbance starts at the fuselage nose at $\tau = 0$.

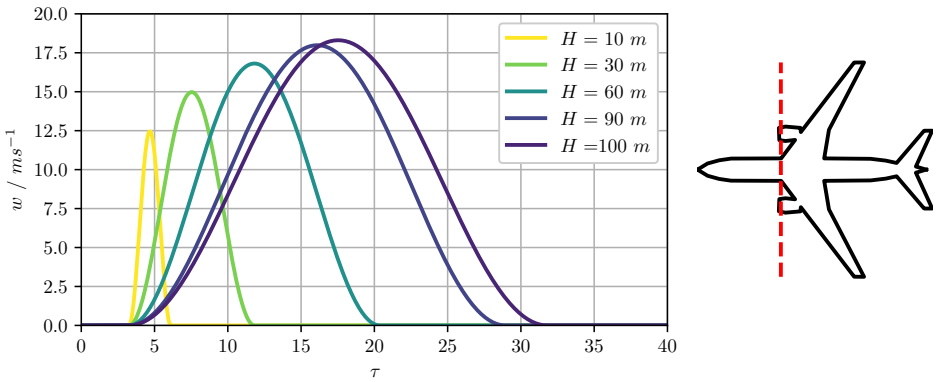

Figure 2: Gust speeds at 10668 m ($F_g = 1$) at the intersection of the wings leading edge and the fuselage versus non-dimensional convection time .

3.7 Gust loads process

For the time integration, the equation of motion Eq. 1 is written as a first order differential equation (ODE) which is then solved with a linear multi-step method. At each time step, the gust disturbance velocities are updated in the mesh, the motion (q_h, $\dot{q}_h$) is updated and the CFD solver is called for one time step. Then, the generalized aerodynamic loads are calculated and the state derivative return to the ODE integrator. It should be kept in mind that no active control is used, so the simulations are open-loop gust encounter simulations.

The responses of full aeroelastic system are time-linearized for each gust gradient using gust amplitudes of $w_g = 0.1\,\mathrm{m\,s^{-1}}$. This approach is not used to derive a time-linearized system, but allows to scale responses by larger gust amplitudes. The advantage is, that it works robustly for each turbulence model and including many degrees of freedom for the motion is not cumbersome.

4 RESULTS

All gust encounters are computed at an altitude of $10\,668\,\mathrm{m}$, at a transonic Mach number of 0.85. The corresponding true airspeed is $U_\infty = 252.055\,\mathrm{m\,s^{-1}}$.

The results for the trim variables computed by the two different turbulence models differ slightly as shown in Table 2. For both turbulence models, flow separation does not occur. It is observed, that both turbulence models predict almost the same steady lift distribution and pressure distribution, once the trim condition of the steady horizontal flight is satisfied.

Table 2: Trim results for the C8/MTOM case at $A = 10668m$ and $Ma = 0.85$

Turbulence model	$\alpha/\circ$	$\eta_{\text{HTP}}/\circ$	$max(dz)/m$
RSM	2.705	-0.816	1.941
SA	2.727	-0.802	1.948

The time integration is conducted with a 3-step Adams-Moulton scheme using a time step $\Delta t = 1.39\,\text{ms}$ ($\Delta\tau = 0.05$). The dual time stepping of the DLR TAU Code for the unsteady simulation is set to run at minimum 250 inner iterations per time step. The inner iterations must reach an absolute residual of 10^{-6} for C_L and Cm_y based on the past 50 values. Depending on the complexity of the flow during the gust encounter, the number of inner iterations is therefore automatically increased. Given a constant wall-clock-time of 36h on 512 CPUs, each simulation then reaches a different physical time.

Gust encounter simulations are performed for all gust gradients shown in Table 1 with a flight profile factor of $F_g = 1$. Further simulations are conducted for the gradients 60, 90, 100 with additional factors of $F_g \in [0.75, 0.8, 0.85, 0.9]$.

Except for the short gust of $H = 10\,\text{m}$ flow separation is observed over large parts of the outer wing for both turbulence models. The effects are quite similar for all other cases, independent of the flight profile factor and gust gradients ($H \geq 30\,\text{m}$).

Figure 3 shows the time history of the nonlinear, and time-linearized lift coefficient C_L for both turbulence models. The linearized responses predict fairly similar values, which agree well with the nonlinear responses up to a time of $\tau \geq 10$. Both nonlinear simulations predict lower values of C_L compared to the linearized curves and the SA-model predicts smaller values compared to the nonlinear RSM-model. Similar trends have been already presented in [1, 2].

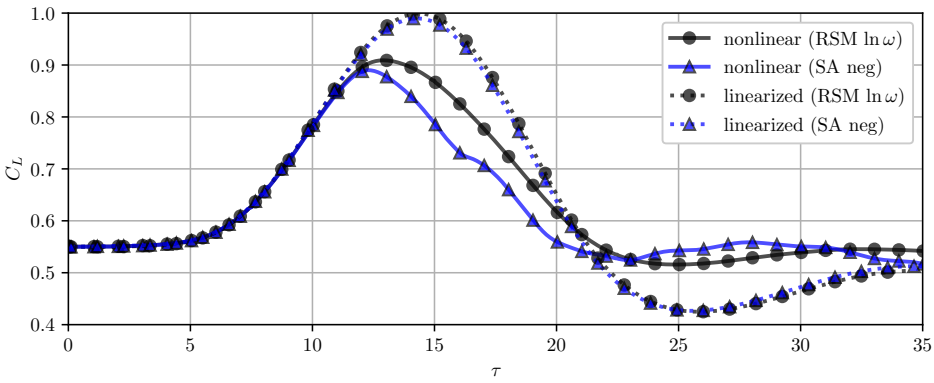

Figure 3: Nonlinear and linearized lift coefficient for a gust: $H = 60\,\text{m}$, $F_g = 1.0$, $w_g = 16.81\,\text{m}\,\text{s}^{-1}$.

The local lift is shown in Figure 4 for the RSM and in Figure 5 for the SA turbulence model. The local lift value (normalized by the local chord) is defined as c_z. While at the inboard sections the local lift seems to be fairly linear, the lift history from $\eta \geq 0.4$ is significantly different between the turbulence models. Due to the flow separation, the time-linearized maximum local lift is not reached by the nonlinear simulations. The results based on the RSM show an ordered

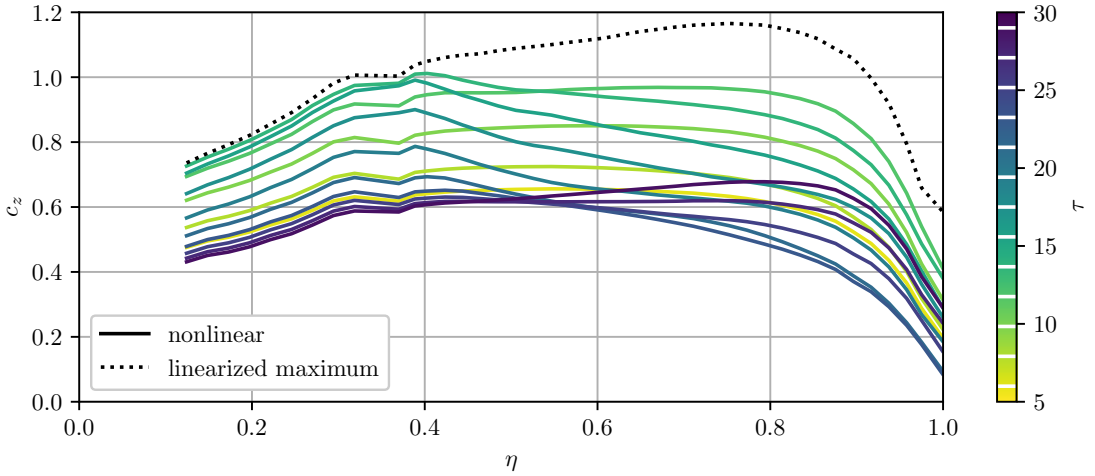

Figure 4: Time slices of the normalized lift distribution for the RSM and a gust defined by: $H = 60\,\mathrm{m}$, $F_g = 1.0$, $w_g = 16.81\,\mathrm{m\,s^{-1}}$.

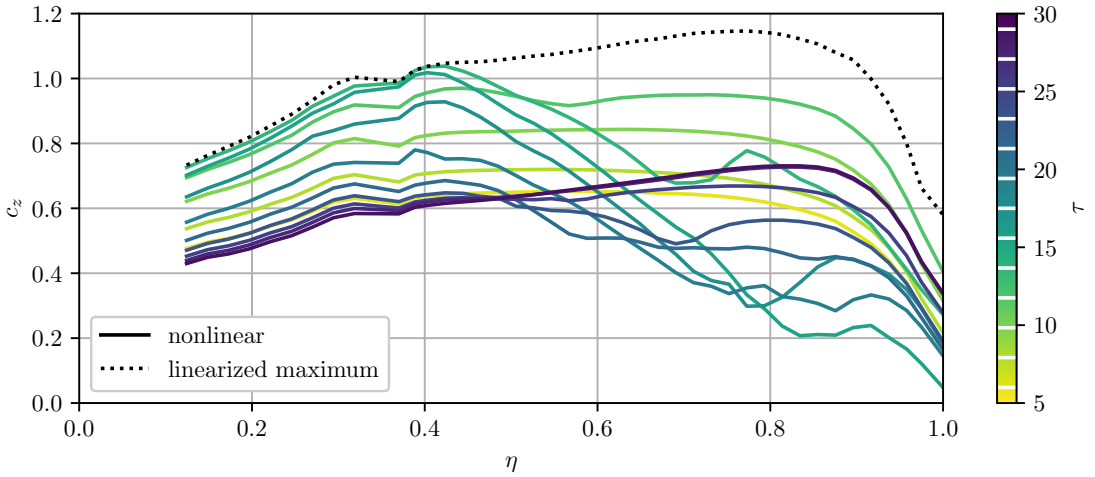

Figure 5: Time slices of the normalized lift distribution for the SA turbulence model and a gust defined by: $H = 60\,\mathrm{m}$, $F_g = 1.0$, $w_g = 16.81\,\mathrm{m\,s^{-1}}$.

and continuously decreasing behavior of the local lift in space and time. The SA turbulence model predicts a much more dynamic behavior of the local lift, which seems to break down from $\eta = 0.5$ to the tip in time.

The flow separation is visualized by skin friction lines on the upper surface of the wing for a time of $\tau = 15.5$ in Figure 6. The flow separation determined by the RSM covers mainly the rear part of the wing. At the inboard section, the SA model predicts a similar pressure distribution but vast parts of the outboard wing shows flow separation and a shock system close to the leading edge. This difference between RSM and SA was observed for all cases with strong flow separation. A similar pattern is shown in [2] for the two turbulence models.

Further insights are provided in Figure 7 which shows pressure slices at different wing stations ($\eta \in [0.20, 0.40, 0.61, 0.81]$) and snapshots of time.

At $\eta = 0.20$, the temporal change of the pressure is very similar for both turbulence models. The amplitudes increase during the gust encounter and the shock moves towards the trailing edge and then returns to the initial position. Further outboard at $\eta = 0.40$, the overall behavior is

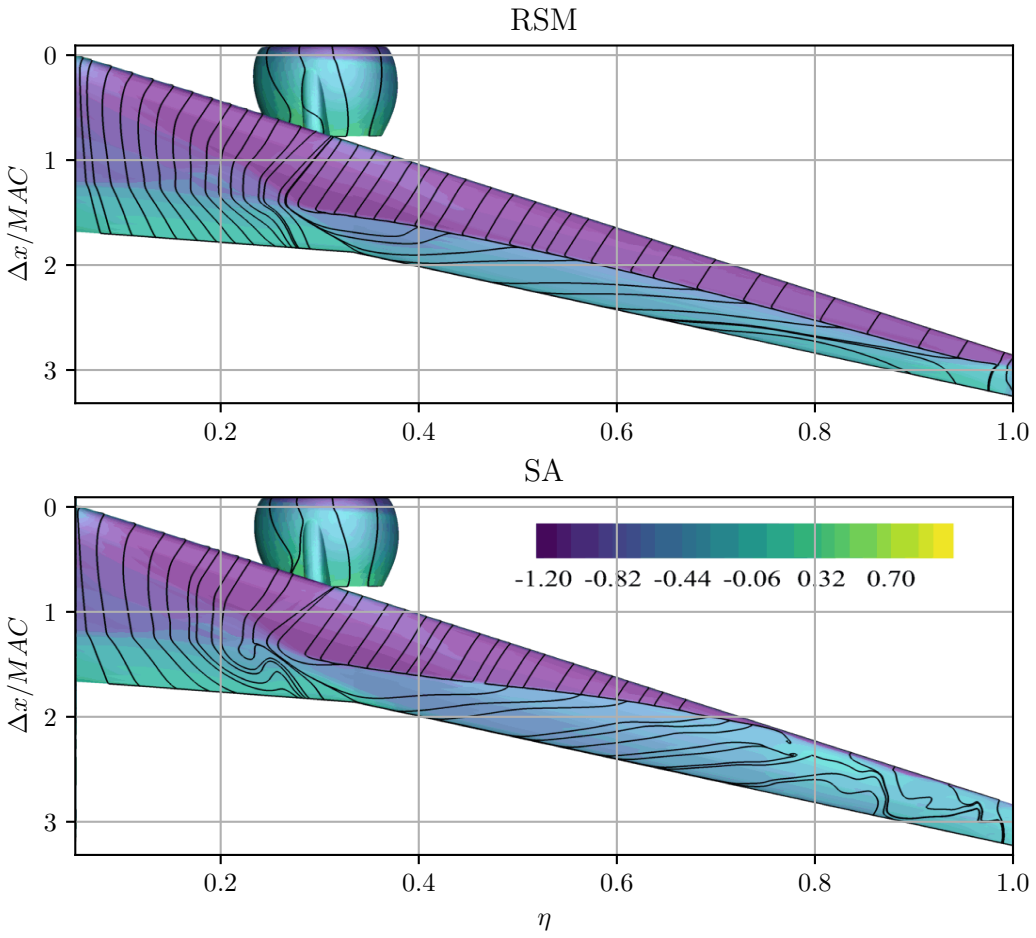

Figure 6: Visualization of the flow separation by skin friction lines for RSM (top) and SA (bottom) turbulence models at $\tau = 15.5$ of a gust defined by: $H = 60\,\mathrm{m}$, $F_g = 1.0$, $w_g = 16.81\,\mathrm{m\,s^{-1}}$.

similar, but the SA model indicates a higher rear-loading (see Figure 7). Even further outboard at $\eta = 0.61$, the SA model shows an inverse shock motion which only shortly moves towards the trailing edge, but then suddenly jumps to 30% of the chord. In contrast, the pressure profile of the RSM remains on a high plateau and the shock motion remains at 60% of the chord. Towards the wing tip at $\eta = 0.81$, the SA model shows a drastic motion of the shock to the leading edge and back. So far outboard, the shock motion of the RSM covers a vast range from 40% to 80% of the chord. Also, the double shock system, which was discussed in [2] can be observed. However, here the shock system starts at a single shock and then falls back to a two-shock system.

With the local pressure, the normal vectors and the segment length, the local aerodynamic section forces and moments cm_y are integrated at the loads reference axis. The coefficients are normalized by the local chord and the gust amplitude. The time histories for the local aerodynamic lift and moment are shown for the same gust and the same stations in Figure 8. First of all, the dotted lines show responses to the gust with a small amplitude of $w_g = 0.1\,\mathrm{m\,s^{-1}}$. This response shows to be in good agreement between both turbulence models, for both the lift and the moment, which is consistent with the global lift in Figure 3. This was observed for all gust gradients, only slight changes in the local moment coefficients appeared.

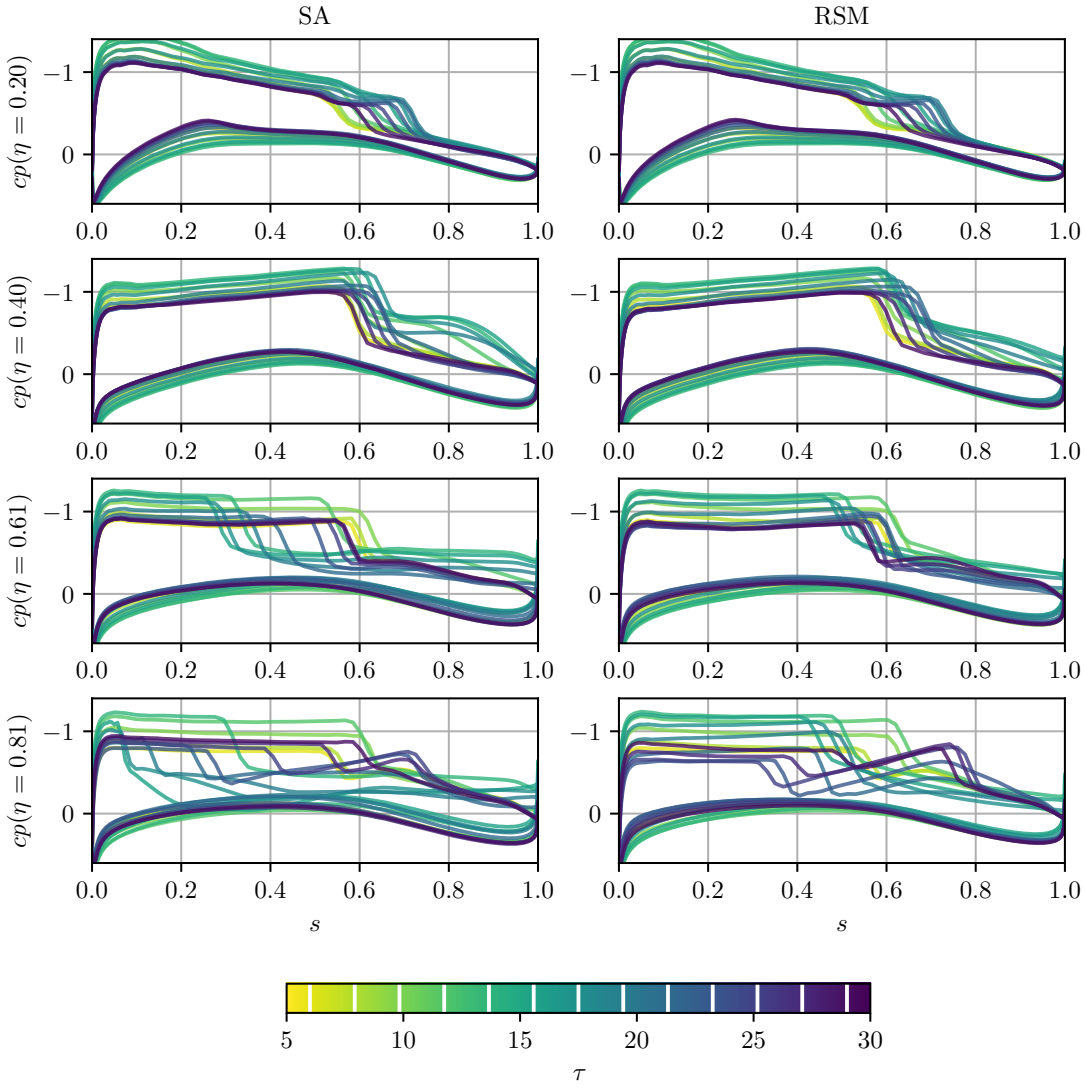

Figure 7: Pressure coefficients at various spanwise locations and different time steps based on the SA turbulence model (left) and RSM (right) for a gust ($H = 60\,\mathrm{m}$, $F_g = 1.0$, $w_g = 16.81\,\mathrm{m\,s^{-1}}$).

For this configuration, starting from a trimmed solution and fully attached flow it is expected that linearized aerodynamics based on both turbulence models should be similar.

The nonlinear and the linear curves at the inner sections ($\eta \in [0.2, 0.4]$) show also good agreement. The moment is slightly changed, due to the shock motion towards the trailing edge at $\eta = 0.20$. The pressure increase behind the shock at $\eta = 0.40$ leads to a significant reduction of the moment. However, the flow separation at the outboard sections ($\eta \in [0.61, 0.81]$) causes a strong reduction in local lift and the plots reveal larger differences between the turbulence models. The local lift shows a more triangular shape for the RSM. In contrast to the smooth curves of the RSM , the SA turbulence model results in a more fluctuating time history with a higher frequency content. This pattern is observed for all gust gradients $\geq 30\,\mathrm{m}$.

The local forces at the wingtip excite a broad range of structural modes for the SA turbulence model, which can be seen for the integrated shear forces of the inertial loads at the wing root in Figure 9. The figure shows on the left the aerodynamic shear force and on the right the inertial shear force. The dashed lines indicate simulations with a reduced set of generalized coordinates (modes 3,5,7) to highlight the excitation of the higher modes. For those results, only three de-

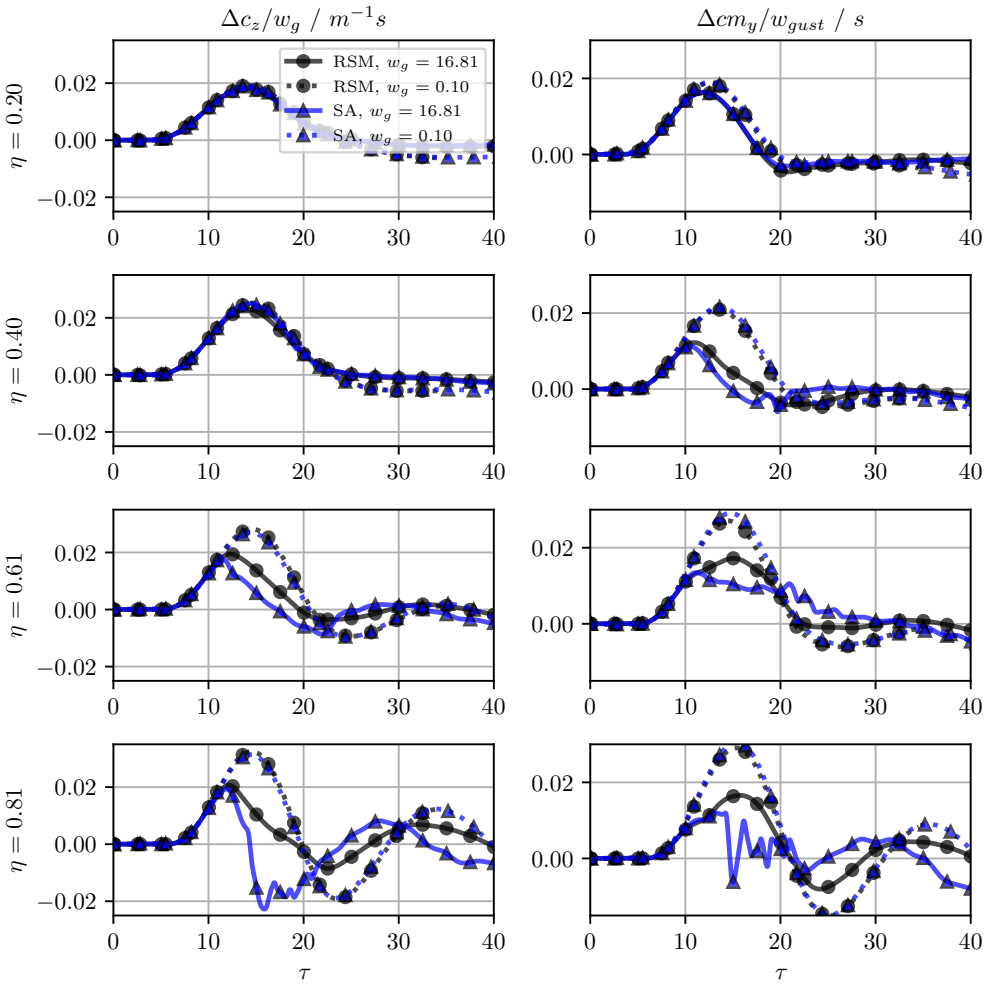

Figure 8: Time history of normalized increments for the local lift (left) and local moment (right) due to a gust ($H = 60\,\mathrm{m}$) for different turbulence models at various spanwise locations (rows).

grees of freedom are considered for pitch, heave and the first bending mode ($f_7 = 1.062\,\mathrm{Hz}$). The aerodynamic loads (left) seem to be very similar for the simulations with different degrees of freedom up to $\tau < 25$. The curves for the aerodynamic loads of the SA turbulence model look very similar to those of the RSM , as if the only difference is caused by an earlier start of the flow separation process. Thus, looking only at the integral aerodynamic loads could lead

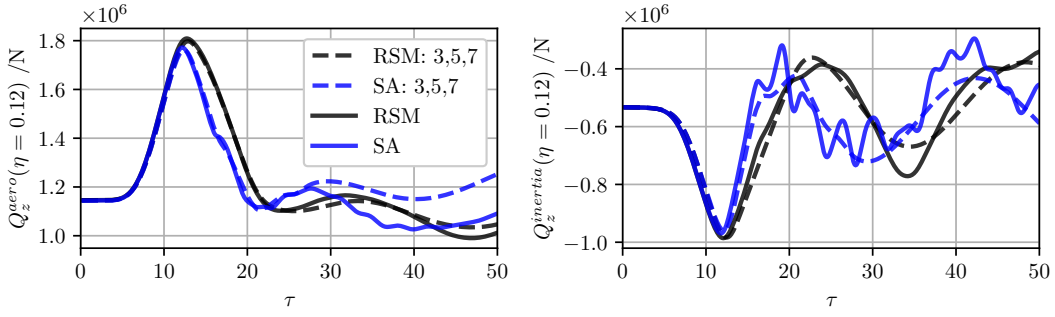

Figure 9: Time history of the aerodynamic (left) and inertial shear (right) at the wing root due to a gust ($H = 60\,\mathrm{m}$, $F_g = 1.$, $w_g = 16.81\,\mathrm{m\,s^{-1}}$) for different turbulence models and different structural degrees of freedom.

to the assumption that the turbulence models predict similar aerodynamic loads. However, the spatial distribution and temporal behavior are significantly different and cause different structural responses. The inertial loads (right) show an earlier deviation from $\tau > 15$ and a similar frequency content for the dashed lines and the solid black line for the RSM. The fast changing aerodynamic behavior of the SA turbulence model excites higher structural frequencies (solid blue line). So when using only three degrees of freedoms (low frequencies) for the motion, the global aerodynamic responses and the structural responses appear to be similar for the turbulence models. However, the dynamic behavior of the distributed aerodynamic forces are significantly different.

The bending moment M_x, torsion moment M_y and shear forces Q_z are integrated cut loads in the coordinate system of the loads reference axis. Also the times at which the maximum values occur are different between the aerodynamic solutions (nonlinear vs. linear, RSM vs. SA). It should be kept in mind, that all extreme values of different load components are not correlated in time as well. For example, the maximum aerodynamic root bending moment occurs at a different time step as the torsional moment. The integrated loads consist of the steady and the dynamic increment as well as the aerodynamic loads and the inertial loads.

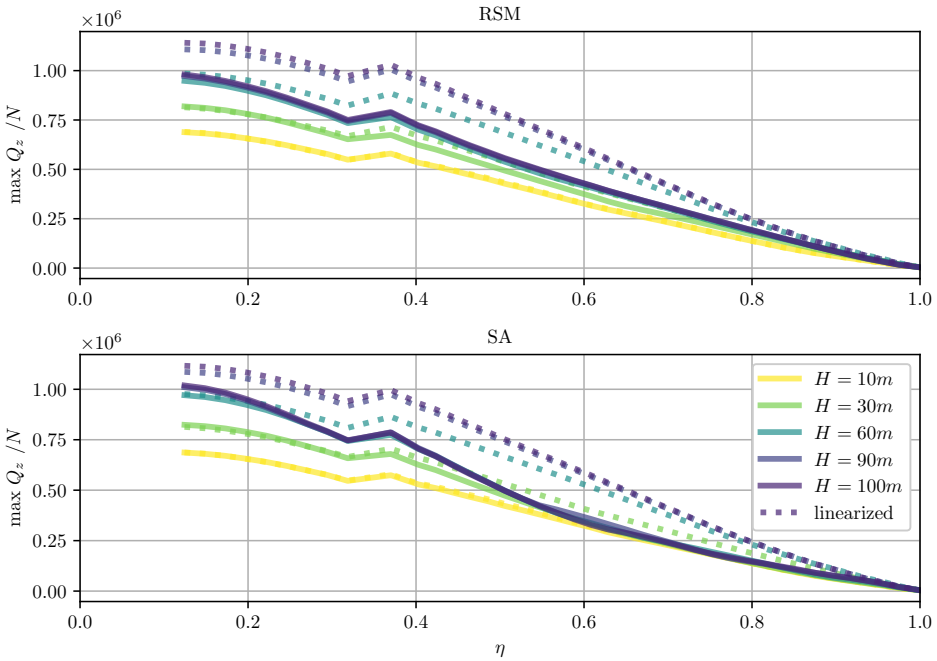

Figure 10: Spanwise distribution of the maximum integrated shear force for the different gust gradients ($F_g = 1.0$) and turbulence models: RSM (top) and SA (bottom).

The spanwise distributions of the shear forces show a significant reduction of loads for the larger gust gradients compared to the time-linearized solution in Figure 10. Towards the wing root, the small to medium reach the value of the time-linearized maximum. The spanwise distribution of the maximum integrated bending moment is shown in Figure 11. The linearized solution predicts a much higher bending moment over the entire span for gust gradients $H \geq 30\,\mathrm{m}$. A significant reduction of the torsion moment over the entire span can be seen for the nonlinear solution compared to the linearized maximum in Figure 12.

The error between the nonlinear and the linearized solution is normalized by the linearized value

$$\bar{e} := \frac{max(L^{nonlin}) - max(L^{lin})}{max(L^{lin})} 100\%. \tag{4}$$

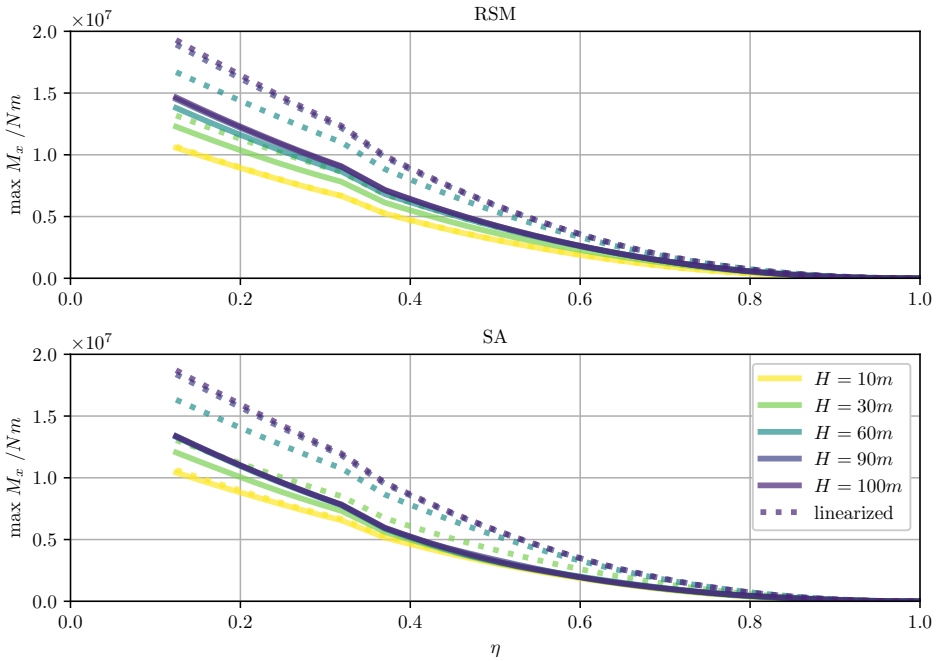

Figure 11: Spanwise distribution of the maximum integrated bending moment for the different gust gradients ($F_g = 1.0$) and turbulence models: RSM (top) and SA (bottom).

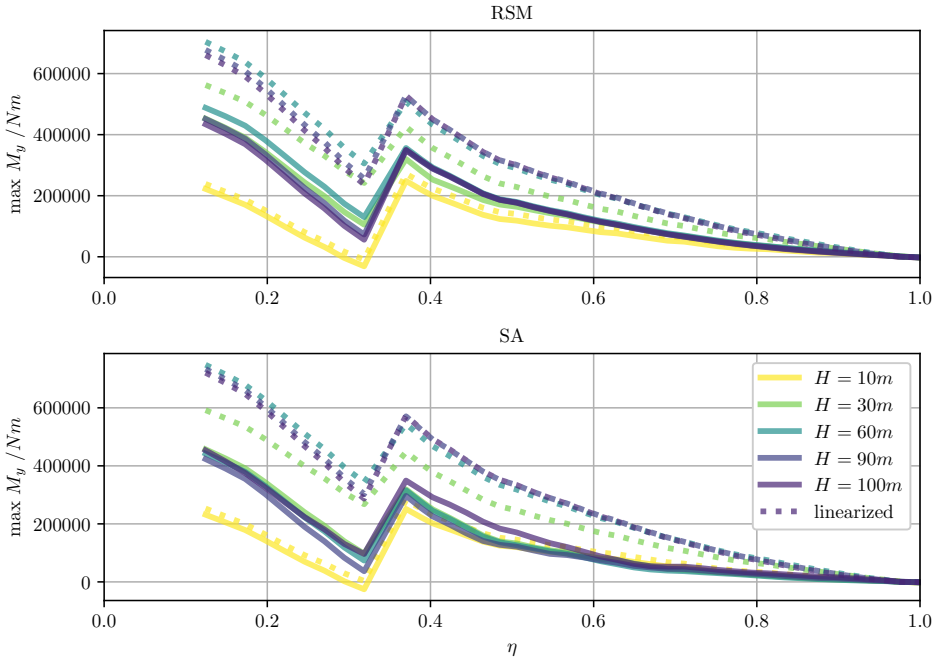

Figure 12: Spanwise distribution of the maximum integrated torsion moment for the different gust gradients ($F_g = 1.0$) and turbulence models: RSM (top) and SA (bottom).

The errors are shown in Figure 13 for the total loads in the left column and the aerodynamic loads in the right column. The colors are used to indicate the flight profile alleviation factor F_g, which scales the reference gust amplitude. In general, the deviations from the linear solution are very large considering that the quantities are cut loads at the wing root. The reduction of the aerodynamic shear force Q_z^{aero} with increasing gust gradient and gust amplitude agrees with the findings in [2]. Similar to the results of [1] a large reduction of the root bending moment M_x can be observed.

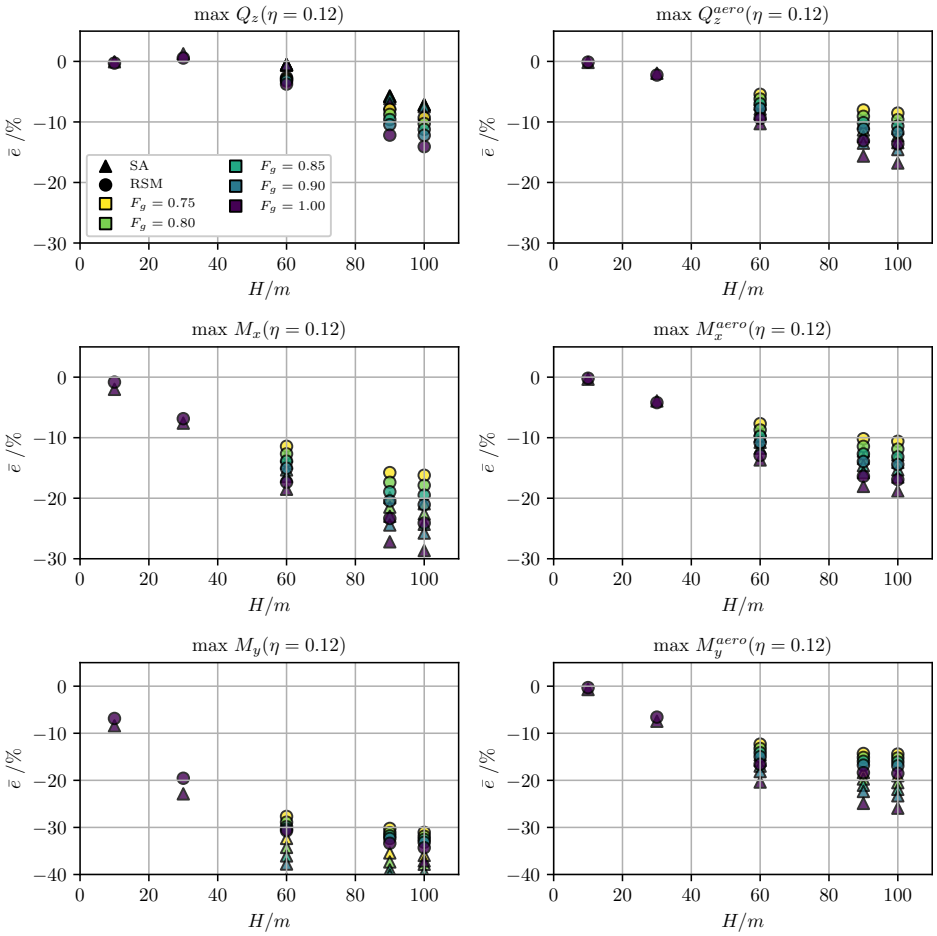

Figure 13: Normalized error vs. gust gradient for maximum integrated loads (shear, bending, torque) for total loads (left) and aerodynamic loads (right).

The small deviation for the short to medium gust gradients for the shear force are small as it is shown for the wing's root. The outboard sections show larger deviations, meaning lower values for the nonlinear results compared to the linear values. This can be seen in Figure 10. For the RSM , the maximum bending moment M_x reduces by $-16\,\%$ to $-24\,\%$ at the largest gust gradient, depending which flight profile factor F_g is applied.

The torque M_y also deviates significantly, which is to be expected if large parts of the outer wing section are affected by the flow separation. The results of the SA turbulence models shows even larger deviations compared to the RSM . The errors of the aerodynamic loads are provided on the right column of the figure. It shows that the SA turbulence model consistently predicts lower aerodynamic loads compared to the RSM .

5 CONCLUSION

Open-loop aeroelastic gust encounter simulations of the CRM have been conducted for a broad range of gusts at transonic speed of $Mach = 0.85$ at an altitude of $10\,668\,\mathrm{m}$. The negative Spalart-Allmaras and the RSM SSG/LLR-$\ln\omega$ turbulence models have been used.

The time-linearized responses between the two turbulence models are very similar. Therefore, it is expected that a time linearization of any of the turbulence models is a good option, as long as the steady flow does not show larger areas of separated flow.

In this work, the SA turbulence model predicts a fast motion of the shock and a strongly changing region of detached flow. Consequently, higher structural frequencies are excited. A reduction of the root bending moment by -21% to -29% compared to the linearized solution is found for the largest gust gradients. In general, the fluctuating time histories of the model for the local lift make the SA turbulence model for cases with strong flow separation questionable.

The simulations with the RSM show large regions of flow separation as well, but those are confined in the rear part of the wing. The time histories are smoother and only lower frequent structural responses are excited. A reduction of the root bending moment by -16% to -24% compared to the linearized solution is found for the largest gust gradients.

A generalization of the findings is difficult, as the results depend for example on the geometry, the flight point, the steady solution, the turbulence model, the mass configurations and flight control. Therefore, more mass configurations, flight points and different aircraft will be investigated in the future with and without flight control.

6 REFERENCES

[1] Kaiser, C., Quero, D., and Nitzsche, J. (2019). Quantification of nonlinear effects in gust load prediction. In *IFASD 2019 - International Forum on Aeroelasticity and Structural Dynamics*.

[2] Friedewald, D. (2023). Large-Amplitude Gusts on the NASA Common Research Model. *Journal of Aircraft*. doi:10.2514/1.C037198.

[3] Vassberg, J., Dehaan, M., Rivers, M., et al. (2008). Development of a Common Research Model for Applied CFD validation studies. In *26th AIAA Applied Aerodynamics Conference*. American Institute of Aeronautics and Astronautics. doi:10.2514/6.2008-6919.

[4] Klimmek, T. (2014). Parametric Set-Up of a Structural Model for FERMAT Configuration for Aeroelastic and Loads Analysis. *Journal of Aeroelasticity and Structural Dynamics*, 3(2), 31–49.

[5] Keye, S., Klimmek, T., Abu-Zurayk, M., et al. (2017). Aero-Structural Optimization of the NASA Common Research Model. In *18th AIAA/ISSMO Multidisciplinary Analysis and Optimization Conference*. American Institute of Aeronautics and Astronautics. doi: 10.2514/6.2017-4145.

[6] Feldwisch, J. and Bauer, M. (2023). UltraFLoads: A Simulation Suite and Framework for High-Fidelity Flight Loads. *Aerospace*, 10(3). ISSN 2226-4310. doi: 10.3390/aerospace10030273.

[7] Reimer, L., Heinrich, R., Geisbauer, S., et al. (2021). Virtual Aircraft Technology Integration Platform: Ingredients for Multidisciplinary Simulation and Virtual Flight Testing. In *AIAA SciTech Forum*. Virtual Event.

[8] Meinel, M. and Einarsson, G. O. (2010). The FlowSimulator framework for massively parallel CFD applications. In *PARA2010*. Reykjavik, Island.

[9] Gerhold, T. (2005). Overview of the Hybrid RANS Code TAU. In N. Kroll and J. K. Fassbender (Eds.), *MEGAFLOW - Numerical Flow Simulation for Aircraft Design*. Berlin, Heidelberg: Springer Berlin Heidelberg. ISBN 978-3-540-32382-2, pp. 81–92.

[10] Schwamborn, D., Gerhold, T., and Heinrich, R. (2006). The DLR TAU-code: Recent applications in research and industry. In *ECCOMAS CFD 2006: Proceedings of the European Conference on Computational Fluid Dynamics*. Egmond aan Zee, The Netherlands.

[11] Eisfeld, B. and Brodersen, O. (2005). Advanced Turbulence Modelling and Stress Analysis for the DLR-F6 configuration. In *23rd AIAA Applied Aerodynamics Conference*, vol. 23rd AIAA Applied Aerodynamics Conference. Toronto, Ontario Canada: AIAA. doi: 10.2514/6.2005-4727.

[12] Braun, S. (2019). Implementation of a $\ln(\omega)$-based SSG/LRR Reynolds Stress Model into the DLR-TAU Code. Tech. rep., Deutsches Zentrum für Luft- und Raumfahrt e.V.

[13] Allmaras, S., Johnson, F., and Spalart, P. (2012). Modifications and clarifications for the implementation of the Spalart-Allmaras turbulence model. In *Seventh International Conference on Computational Fluid Dynamics (ICCFD7)*. Hawaii, pp. 1–11.

[14] Tinoco, E. N., Brodersen, O. P., Keye, S., et al. (2018). Summary Data from the Sixth AIAA CFD Drag Prediction Workshop: CRM Cases. *Journal of Aircraft*, 55(4), 1352–1379.

[15] European Union Aviation Safety Agency. *Certification Specifications and Acceptable Means of Compliance for Large Aeroplanes, CS-25*. 28.

COPYRIGHT STATEMENT